Air Force Institute of Technology

AFIT Scholar

Faculty Publications

12-30-2016

Generation of Vector Partially Coherent Optical Sources Using Phase-Only Spatial Light Modulators

Milo W. Hyde IV
Air Force Institute of Technology

Santasri Bose-Pillai
Air Force Institute of Technology

David G. Voelz
New Mexico State University

Xifeng Xiao
New Mexico State University

Generation of Vector Partially Coherent Optical Sources Using Phase-Only Spatial Light Modulators

Milo W. Hyde IV[*]

Department of Electrical and Computer Engineering, Air Force Institute of Technology,
2950 Hobson Way, Dayton, Ohio 45433, USA

Santasri Bose-Pillai[†]

Department of Engineering Physics, Air Force Institute of Technology,
Dayton, Ohio 45433, USA

David G. Voelz[‡] and Xifeng Xiao[§]

Klipsch School of Electrical and Computer Engineering, New Mexico State University,
MSC 3-O, Goddard Annex 160B, Las Cruces, New Mexico 88003, USA

A simple and flexible optical system for generating electromagnetic or vector partially coherent sources or beams is presented. The alternative design controls field amplitude (beam shape), coherence, and polarization using only spatial light modulators. This improvement makes the apparatus simpler to construct and significantly increases the flexibility of vector partially coherent source generators by allowing many different types of sources to be produced without changing the physical setup. The system's layout and theoretical foundations are thoroughly discussed. The utility and flexibility of the proposed system are demonstrated by producing a vector Schell-model and non-Schell-model source. The experimental results are compared to theoretical predictions to validate the design. Lastly, design aspects, which must be considered when building a vector partially coherent source generator for a specific application, are discussed.

I. INTRODUCTION

Motivated by Wolf's seminal work on coherence and polarization [1,2], research involving vector or electromagnetic partially coherent sources has become quite popular [3–6]. Their widespread appeal stems from the fact that, by simply manipulating spatial coherence, the source's resulting shape and polarization can be precisely controlled. Numerous researchers have designed vector partially coherent sources for applications such as free-space and underwater optical communications [7–16], remote sensing [17,18], optical scattering [19–29], and particle manipulation and trapping [30–33].

As one might expect, considering their many uses, optical systems to generate vector partially coherent sources have also been developed. The most straightforward and therefore popular design uses a Mach-Zehnder interferometer (MZI) consisting of polarizing beam splitters (PBSs) to split light from a common source into its vertical and horizontal polarization components [5,6,11,34–39]. In each leg of the MZI, the amplitude (beam shape) and coherence of each field component are controlled using absorbing (amplitude) filters and ground-glass diffusers [6,30–33,35,36,40,41] or spatial light modulators (SLMs) [5,11,34,37,38,42,43], respectively. While intuitive, the use of separate optical components to control beam shape and coherence complicates the optical setup (alignment, system footprint or size, et cetera) and limits the types of vector partially coherent sources that can be generated (the system's flexibility).

Designs that rely on ground-glass diffusers to affect coherence are generally limited to producing Schell-model sources [2,5,44,45]. The use of SLMs can ameliorate this limitation; however, to the authors' knowledge, they have never been used to produce vector non-Schell-model sources. The most limiting aspect of existing designs is the use of amplitude filters to control beam shape. Amplitude filters adversely affect the flexibility of the system, considering that every new source requires a new set of filters.

In this paper, a simple and flexible design for generating vector partially coherent sources is presented. Like existing designs, the proposed system uses a MZI where, in each interferometer leg, the beam shape and coherence of the field's horizontal and vertical polarization components are controlled separately. In contrast with existing designs, the apparatus presented here uses only SLMs to control

[*]milo.hyde@afit.edu
[†]Formerly known as Santasri Basu.
santasri.basu.ctr.in@afit.edu
[‡]davvoelz@nmsu.edu
[§]xixiao@nmsu.edu

coherence and beam shape. This improvement permits many different types of sources to be generated without physically changing the apparatus.

In Sec. II, the system is presented and described in detail. Section III presents the theory necessary for understanding how the apparatus creates vector partially coherent sources. Section IV demonstrates the flexibility of the proposed design by experimentally producing both vector non-Schell-model and Schell-model sources. The experimental results are compared to theoretical predictions to validate the system. Lastly, key aspects of the proposed approach, which must be considered when designing a system for a specific application, are discussed.

II. APPARATUS DESCRIPTION

A schematic of the vector partially coherent source generator is shown in Fig. 1. Light is emitted from a

FIG. 1. Schematic of the proposed vector partially coherent source generator. The acronyms used in the figure are 350-mm lens (*L*1), 375-mm lens (*L*2), 1500-mm lens (*L*3), mirror (*M*), half-wave plate (HWP), beam expander (BE), polarizing beam splitter (PBS), iris (*I*), and spatial light modulator (SLM). The polarization state of the light passing through the apparatus is denoted by two-sided arrows (horizontal polarization) and dotted circles (vertical polarization). When both symbols are present, the light is in a general polarization state, i.e., polarized, partially polarized, or unpolarized.

HeNe laser (632.8 nm) and then expanded. The laser light then traverses a half-wave plate (HWP) before being split along two paths using a PBS. The HWP is used to rotate the angle of polarization (AOP) of the linearly polarized laser light to 45° such that the PBS splits the power equally between the vertical and horizontal legs—so named because of the polarization state that is controlled on that leg.

After passing through the PBS, the light in both legs is incident on reflective, phase-only SLMs. The SLMs used here are Boulder Nonlinear Systems (BNS) model P512-0635 SLMs [46]. Since the BNS SLMs control only vertically polarized light, a HWP is used immediately after the PBS to rotate the vertical leg's AOP 90°. Note that all beam shaping, phasing, and relative amplitude control on the vertical and horizontal legs is performed using the SLMs. This field control is accomplished using the modified phase-screen (MPS) technique [47], which is briefly reviewed in the next section.

The light reflected from the SLMs is scattered into multiple diffraction orders. Here, the desired vertical- and horizontal-leg field instances are produced in the first diffraction orders. Thus, spatial filters (4*f* system plus an iris) are utilized on each leg to isolate the desired first orders.

The physical layout of the system results in the vertical leg being 100 mm longer than the horizontal leg when measured from the SLMs (the same difference is approximately 45 mm when measured from the laser). To place the output planes of both spatial filters at *L*3, the horizontal and vertical leg lenses (*L*1 and *L*2, respectively) have focal lengths of 350 and 375 mm, respectively.

Note that the coherence length of the source must be considered when designing the system. If the optical path difference (OPD) between the horizontal and vertical legs is greater than the coherence length of the source, only partially coherent beams with diagonal cross-spectral density (CSD) matrices can be generated. The coherence length of the HeNe laser used here is approximately 300 mm; therefore, the 45-mm difference between the legs of the MZI is not a problem.

After passing through the spatial filters, the light in the vertical and horizontal legs is recombined using a PBS. Note that the light in the horizontal leg first transits a HWP to rotate its polarization state from vertical (the SLM control state) to horizontal. The recombined light is then incident on *L*3—a 1500-mm lens located at the effective source plane of the apparatus. The lens produces the far-zone irradiance pattern of the field, which is subsequently recorded by a Lumenera Lw135RM camera [48] placed at the focus of *L*3.

III. METHODOLOGY

A vector partially coherent source is completely described by the elements of its CSD matrix:

$$\mathbf{W}(\boldsymbol{\rho}_1,\boldsymbol{\rho}_2,\omega)$$

$$= \begin{bmatrix} W_{xx}(\boldsymbol{\rho}_1,\boldsymbol{\rho}_2,\omega) & W_{xy}(\boldsymbol{\rho}_1,\boldsymbol{\rho}_2,\omega) \\ W_{yx}(\boldsymbol{\rho}_1,\boldsymbol{\rho}_2,\omega) & W_{yy}(\boldsymbol{\rho}_1,\boldsymbol{\rho}_2,\omega) \end{bmatrix}$$

$$= \begin{bmatrix} \langle E_x(\boldsymbol{\rho}_1,\omega)E_x^*(\boldsymbol{\rho}_2,\omega)\rangle & \langle E_x(\boldsymbol{\rho}_1,\omega)E_y^*(\boldsymbol{\rho}_2,\omega)\rangle \\ \langle E_y(\boldsymbol{\rho}_1,\omega)E_x^*(\boldsymbol{\rho}_2,\omega)\rangle & \langle E_y(\boldsymbol{\rho}_1,\omega)E_y^*(\boldsymbol{\rho}_2,\omega)\rangle \end{bmatrix}, \quad (1)$$

where E_i is the ith component of the electric field, W_{ij} is the CSD function of the ith and jth field components, $\boldsymbol{\rho} = \hat{\mathbf{x}}x + \hat{\mathbf{y}}y$, and ω is the radian frequency [2,5]. Note that, in expressing $\mathbf{W}$ as a function of a single frequency ω, it has been assumed that the random optical field is wide-sense stationary. Hereafter, the dependence of the CSD matrix, the CSD functions, and the optical fields on ω is suppressed.

In this work, W_{ij}'s of the form

$$W_{ij}(\boldsymbol{\rho}_1,\boldsymbol{\rho}_2) = \sqrt{S_i(\boldsymbol{\rho}_1)}\sqrt{S_j(\boldsymbol{\rho}_2)}\mu_{ij}(\boldsymbol{\rho}_1,\boldsymbol{\rho}_2) \quad (2)$$

are germane. In Eq. (2), S_i is the spectral density of the ith field component and μ_{ij} is the cross-correlation function of the ith and jth components. It is required that $\mu_{ij} = \mu_{ji}^*$ [2,5]. If μ_{ij} can be expressed solely as a function of $\boldsymbol{\rho}_1 - \boldsymbol{\rho}_2$, then W_{ij} in Eq. (2) takes the Schell-model form [2,5,44,45]. To demonstrate the flexibility of the apparatus in Fig. 1, both a non-Schell-model and a Schell-model source are generated (the results are shown in Sec. IV). For now, the analysis continues with the general CSD function given in Eq. (2).

A. Modified phase-screen technique

An instance of a MPS field takes the form [47]

$$\mathbf{E}^{\mathrm{MPS}}(\boldsymbol{\rho}) = \hat{\mathbf{x}}\sqrt{S_x(\boldsymbol{\rho})}\exp\left(j\{\arg[T_x(\boldsymbol{\rho})] + \alpha_x\}\right)$$
$$+ \hat{\mathbf{y}}\sqrt{S_y(\boldsymbol{\rho})}\exp\left(j\{\arg[T_y(\boldsymbol{\rho})] + \alpha_y\}\right), \quad (3)$$

where $j = \sqrt{-1}$, α_i is the phase of the ith field component, and T_i is the complex transmittance screen for the ith component [49–51]. Taking the vector autocorrelation of Eq. (3) yields

$$W_{ij}^{\mathrm{MPS}}(\boldsymbol{\rho}_1,\boldsymbol{\rho}_2) = \langle E_i^{\mathrm{MPS}}(\boldsymbol{\rho}_1)E_j^{\mathrm{MPS}*}(\boldsymbol{\rho}_2)\rangle$$
$$= \sqrt{S_i(\boldsymbol{\rho}_1)}\sqrt{S_j(\boldsymbol{\rho}_2)}\exp[j(\alpha_i - \alpha_j)]$$
$$\times \langle \exp\{j\arg[T_i(\boldsymbol{\rho}_1)]\}\exp\{-j\arg[T_j(\boldsymbol{\rho}_2)]\}\rangle$$
$$= \sqrt{S_i(\boldsymbol{\rho}_1)}\sqrt{S_j(\boldsymbol{\rho}_2)}\chi_{ij}(\boldsymbol{\rho}_1,\boldsymbol{\rho}_2). \quad (4)$$

Comparing Eq. (4) to Eq. (2) reveals the following desired condition:

$$\chi_{ij}(\boldsymbol{\rho}_1,\boldsymbol{\rho}_2) = \mu_{ij}(\boldsymbol{\rho}_1,\boldsymbol{\rho}_2), \quad (5)$$

which, in general, is never satisfied. However, it can be shown, by numerically computing χ_{ij} using the joint probability density function of speckle phases [52], that $\chi_{ij} \approx \mu_{ij}$, such that the MPS partially coherent source is practically indistinguishable from the true source. This analysis is presented in Ref. [53] and not reproduced here for the sake of brevity. Methods to synthesize T_x and T_y to produce the desired μ_{xx}, μ_{yy}, and μ_{xy}'s are presented next.

B. Screen synthesis

1. Non-Schell-model source

It is now convenient to assume forms for S_i and μ_{ij}. An example of a vector non-Schell-model source, which to the authors' knowledge has never been physically generated before, is an electromagnetic nonuniformly correlated (ENUC) beam [5,54]. Its CSD matrix elements take the form

$$W_{ij}(\boldsymbol{\rho}_1,\boldsymbol{\rho}_2) = A_i\exp\left(-\frac{\rho_1^2}{4\sigma_i^2}\right)A_j\exp\left(-\frac{\rho_2^2}{4\sigma_j^2}\right)$$
$$\times B_{ij}\exp\left\{-\frac{(|\boldsymbol{\rho}_1 - \boldsymbol{\gamma}_i|^2 - |\boldsymbol{\rho}_2 - \boldsymbol{\gamma}_j|^2)^2}{\delta_{ij}^4}\right\}, \quad (6)$$

where A_i and σ_i are the amplitude and the rms width of the ith field component, respectively. Also, in Eq. (6), δ_{ij} is the cross-correlation width, B_{ij} is the complex cross-correlation coefficient, and $\boldsymbol{\gamma}_i$ is a real, two-dimensional vector that shifts the maximum of the correlation function away from the origin. Note that $\delta_{ij} = \delta_{ji}$, $B_{ij} = B_{ji}^*$, $B_{ii} = B_{jj} = 1$, and $|B_{ij}| \leq 1$. In addition to these requirements, the ENUC source must also satisfy the realizability conditions given in Refs. [5,54].

Synthesizing screens that will produce a desired ENUC source can be accomplished using the Cholesky-factorization approach [55,56]. Assuming an $N_y \times N_x$ computational grid, an instance of T_i is created by

$$\mathbf{T}_i = \mathbf{R}_i\frac{\mathbf{r}_i}{\sqrt{2}}, \quad (7)$$

where $\mathbf{r}_i$ is an $(N_yN_x) \times 1$ vector of zero-mean, unit-variance, circular complex Gaussian random numbers and $\mathbf{T}_i$ is the $(N_yN_x) \times 1$ complex screen. Lastly, $\mathbf{R}_i$ is an $(N_yN_x) \times (N_yN_x)$ lower triangular matrix formed from the Cholesky decomposition of μ_{ii}, namely,

$$\boldsymbol{\mu}_{ii} = \mathbf{R}_i^T\mathbf{R}_i, \quad (8)$$

where $\boldsymbol{\mu}_{ii}$ is the $(N_yN_x) \times (N_yN_x)$ matrix created by evaluating μ_{ii} [the exponential on the second line of

Eq. (6)] at all combinations of points (x_1, y_1) and (x_2, y_2) making up the discrete grid.

Generating T_x and T_y using Eq. (7) will produce an ENUC source with the desired μ_{xx} and μ_{yy}. The statistical relationship between T_x and T_y, particularly the cross-correlation of T_x and T_y, determines μ_{xy}:

$$\langle \boldsymbol{T}_x \boldsymbol{T}_y^\dagger \rangle = \left\langle \mathbf{R}_x \frac{\boldsymbol{r}_x}{\sqrt{2}} \left(\mathbf{R}_y \frac{\boldsymbol{r}_y}{\sqrt{2}} \right)^\dagger \right\rangle$$

$$= \frac{1}{2} \mathbf{R}_x \mathbf{R}_y^T \langle \boldsymbol{r}_x \boldsymbol{r}_y^\dagger \rangle, \qquad (9)$$

where $\dagger$ is the Hermitian transpose. The moment $\langle \boldsymbol{r}_x \boldsymbol{r}_y^\dagger \rangle = 2|B_{xy}|$, simplifying Eq. (9) to

$$\langle \boldsymbol{T}_x \boldsymbol{T}_y^\dagger \rangle = |B_{xy}| \mathbf{R}_x \mathbf{R}_y^T. \qquad (10)$$

The right-hand side of Eq. (10) should equal the Cholesky factorization of $|\mu_{xy}|$. In general, it does not; however, there are two cases where it does:

(1) If $B_{xy} = 0$, δ_{xy} is irrelevant, T_x and T_y are statistically independent, and one is free to choose δ_{xx} and δ_{yy}.

(2) If $B_{xy} \neq 0$, then $\delta_{xx} = \delta_{yy} = \delta_{xy}$ and $\boldsymbol{\gamma}_x = \boldsymbol{\gamma}_y$.

Using the Cholesky-factorization approach outlined above, any vector partially coherent source can be produced. Unfortunately, this flexibility comes at a great cost. Computing Cholesky factors is very computationally intensive—the number of operations is $O(n^3)$ [56]. In addition, the matrix $\boldsymbol{\mu}_{ii}$ is typically very large, requiring a great deal of computer memory to store. For example, synthesizing a screen for a 512×512 SLM (the same size as the BNS SLMs used here) requires a staggering 262, 144 × 262, 144 $\boldsymbol{\mu}_{ii}$. To produce T_x and T_y for the ENUC experiments (the results are presented below), $\boldsymbol{\mu}_{xx}$ and $\boldsymbol{\mu}_{yy}$ are calculated on 128×128 down-sampled versions of the horizontal- and vertical-leg SLMs. From these down-sampled $\boldsymbol{\mu}_{xx}$ and $\boldsymbol{\mu}_{yy}$, $\mathbf{R}_x$ and $\mathbf{R}_y$ are computed. The screens are then synthesized using Eq. (7), reshaped, and interpolated to 512×512.

2. Schell-model source

The Cholesky-factorization approach discussed in the previous section can be used to synthesize screens to produce any type of partially coherent source; however, the approach is very computationally intensive. If the partially coherent beam is a Schell-model source, then a simpler and more computationally efficient technique can be used to synthesize T_x and T_y.

An example of a vector Schell-model source is an electromagnetic multi-Gaussian Schell-model (EMGSM) beam [5,57]. To the authors' knowledge, a general EMGSM beam has never been physically produced before.

The CSD matrix elements of an EMGSM source take the form [5,57]

$$W_{ij}(\boldsymbol{\rho}_1, \boldsymbol{\rho}_2) = A_i \exp\left(-\frac{\rho_1^2}{4\sigma_i^2}\right) A_j \exp\left(-\frac{\rho_2^2}{4\sigma_j^2}\right)$$

$$\times \frac{B_{ij}}{C_0} \sum_{m=1}^{M} \binom{M}{m} \frac{(-1)^{m-1}}{m} \exp\left[-\frac{|\boldsymbol{\rho}_1 - \boldsymbol{\rho}_2|^2}{2m\delta_{ij}^2}\right], \qquad (11)$$

where the normalization constant C_0 is

$$C_0 = \sum_{m=1}^{M} \binom{M}{m} \frac{(-1)^{m-1}}{m}. \qquad (12)$$

The other symbols were defined previously. The same requirements on δ_{ij} and B_{ij} stipulated above apply to EMGSM sources as well. In addition, EMGSM sources must also satisfy the realizability conditions given in Refs. [5,57].

Since an EMGSM beam is a Schell-model source, T_x and T_y can be generated using the Monte Carlo spectral method. This technique has been described in the literature many times [5,49–51,58,59]; therefore, only the key relations are included here. An instance of T_i can be synthesized by

$$T_i[k, l] = \sum_{p,q} r_i[p, q] \sqrt{\frac{\Phi_{ii}[p, q]}{2L_x L_y}}$$

$$\times \exp\left(j \frac{2\pi}{N_x} pk\right) \exp\left(j \frac{2\pi}{N_y} ql\right), \qquad (13)$$

where k, l are the discrete spatial indices of the screen, p, q are the discrete spatial frequency indices, L_x and L_y are the width and height of the grid in meters, and r_i is an $N_y \times N_x$ matrix of zero-mean, unit-variance, circular complex Gaussian random numbers. Lastly, Φ_{ii} is the spatial power spectrum of T_i (the Fourier transform of μ_{ii}), namely,

$$\Phi_{ii}(\boldsymbol{f}) = \frac{2\pi\delta_{ii}^2}{C_0} \sum_{m=1}^{M} \binom{M}{m} (-1)^{m-1} \exp(-2m\pi^2\delta_{ii}^2 f^2), \qquad (14)$$

where $\boldsymbol{f} = \hat{\boldsymbol{x}} f_x + \hat{\boldsymbol{y}} f_y$ is the spatial-frequency vector. Equation (13) is in the form of a discrete inverse Fourier transform; thus, T_i can be synthesized using the fast-Fourier-transform (FFT) algorithm.

Synthesizing T_x and T_y using Eq. (13) will produce an EMGSM source with the desired μ_{xx} and μ_{yy}. To determine the form of μ_{xy}, one must take the cross-correlation of Eq. (13), viz.,

$$\langle T_x[k_1, l_1] T_y^*[k_2, l_2] \rangle = \sum_{p_1, q_1} \sum_{p_2, q_2} \frac{\langle r_x[p_1, q_1] r_y^*[p_2, q_2] \rangle}{2 L_x L_y}$$

$$\times \sqrt{\Phi_{xx}[p_1, q_1] \Phi_{yy}[p_2, q_2]}$$

$$\times \exp\left[j \frac{2\pi}{N_x} (p_1 k_1 - p_2 k_2) \right]$$

$$\times \exp\left[j \frac{2\pi}{N_y} (q_1 l_1 - q_2 l_2) \right]. \quad (15)$$

The moment in Eq. (15) evaluates to $2 |B_{xy}| \delta[p_1 - p_2] \times \delta[q_1 - q_2]$, where δ is the discrete Dirac delta function. Simplifying Eq. (15) further yields

$$\langle T_x[k_1, l_1] T_y^*[k_2, l_2] \rangle = \sum_{p, q} \frac{|B_{xy}|}{L_x L_y} \sqrt{\Phi_{xx}[p, q] \Phi_{yy}[p, q]}$$

$$\times \exp\left[j \frac{2\pi}{N_x} (k_1 - k_2) p \right]$$

$$\times \exp\left[j \frac{2\pi}{N_y} (l_1 - l_2) q \right]. \quad (16)$$

The expression $|B_{xy}| \sqrt{\Phi_{xx} \Phi_{yy}}$ should equal the cross-power spectrum, namely,

$$\Phi_{xy}(f) = |B_{xy}| \frac{2\pi \delta_{xy}^2}{C_0} \sum_{m=1}^{M} \binom{M}{m} (-1)^{m-1}$$

$$\times \exp(-2m\pi^2 \delta_{xy}^2 f^2). \quad (17)$$

Like the ENUC source discussed above, $|B_{xy}| \sqrt{\Phi_{xx} \Phi_{yy}} = \Phi_{xy}$ if (1) $B_{xy} = 0$ or (2) $B_{xy} \neq 0$, then $\delta_{xx} = \delta_{yy} = \delta_{xy}$.

Following the above analysis, any vector Schell-model source can be produced. Depending on the forms of μ_{xx}, μ_{yy}, and μ_{xy}, one may have more freedom in choosing B_{xy}, δ_{xx}, δ_{yy}, and δ_{xy} than in the EMGSM case above. Two such sources are the electromagnetic Gaussian Schell-model (EGSM) [50] and EGSM vortex beams [32].

C. Phase-only MPS field

Recall that in the apparatus in Fig. 1, all phasing and amplitude control is accomplished using phase-only SLMs. In the preceding sections, two methods for synthesizing T_x and T_y to produce partially coherent sources with the desired μ_{xx}, μ_{yy}, and μ_{xy} are discussed. This analysis handles the MPS field component *phases* that are ultimately commanded to the horizontal- and vertical-leg SLMs. What remains is a discussion of how the MPS field component *amplitudes*, namely, $\sqrt{S_x}$ and $\sqrt{S_y}$, are handled.

Amplitude can be controlled using a phase-only SLM by creating a sawtooth phase grating which produces the desired field in the first diffraction order. By manipulating the height of the grating, the field's amplitude can be precisely controlled. The expression relating sawtooth height to the field in the first diffraction order was derived previously [51,60,61]:

$$U(\rho) \approx \text{sinc}\{\pi[1 - h(\rho)]\} \exp\{-j\pi[1 - h(\rho)]\}$$

$$= H(h) \exp[-jP(h)], \quad (18)$$

where h is the height of sawtooth in waves and $\text{sinc}(x) = \sin(x)/x$. Assumed in this relation is that more than four SLM pixels compose each sawtooth.

The vertical- and horizontal-leg phases commanded to the SLMs are

$$\theta_V[k, l] = \arg(\exp\{j[G(h_y) + \arg(T_y) + F(h_y) + \alpha_y]\})$$

$$\theta_H[k, l] = \arg(\exp\{j[G(h_x) + \arg(T_x) + F(h_x) + \alpha_x]\}), \quad (19)$$

where h_x and h_y are found by solving

$$h_i = H^{-1}\left(\sqrt{\frac{S_i}{\max\{S_i, S_j\}}} \right), \quad (20)$$

G is the function that forms the two-dimensional sawtooth phase grating, and F is the function that creates a two-dimensional P. The purpose of F is to remove the "phase aberration" caused by G. Note that $\exp[j(\alpha_x - \alpha_y)] = \exp[j \arg(B_{xy})]$. The desired x and y components of the MPS field are produced in the horizontal and vertical legs' first diffraction orders, respectively.

It should be noted that, in general, the heights of the sawteeth making up the SLM gratings vary spatially; however, all of the sawteeth contain the same number of SLM pixels. The SLM gratings can be formed in any direction—horizontally, vertically, or diagonally.

Figure 2 shows the screen synthesis process. Here, a screen which produces a single instance of E_y of an EMGSM source is synthesized. Step 1 shows the spectral density S_y and correlation function μ_{yy} of the source. The sawtooth grating is determined by the spectral density; thus, steps 2, finding the grating heights h_y [Eq. (20)], and 3, the functions G and F, are grouped under S_y. The phase of the screen is formed from the correlation function—in this case, via the power spectrum. Hence, steps 4, the spatial power spectrum Φ_{yy} [Eq. (14)], and 5, creating an instance of T_y [Eq. (13)], are grouped below μ_{yy}. Lastly, the screen θ_V is produced in step 6 by using Eq. (19). The same process is used to produce an instance of E_x, i.e., to synthesize the horizontal-leg screen θ_H.

Note that if $|B_{xy}| \neq 0$, then T_x and T_y must be synthesized from correlated r_x and r_y [see Eq. (13)]. Since r_x and r_y are Gaussian, this task is a relatively easy one. Most of the
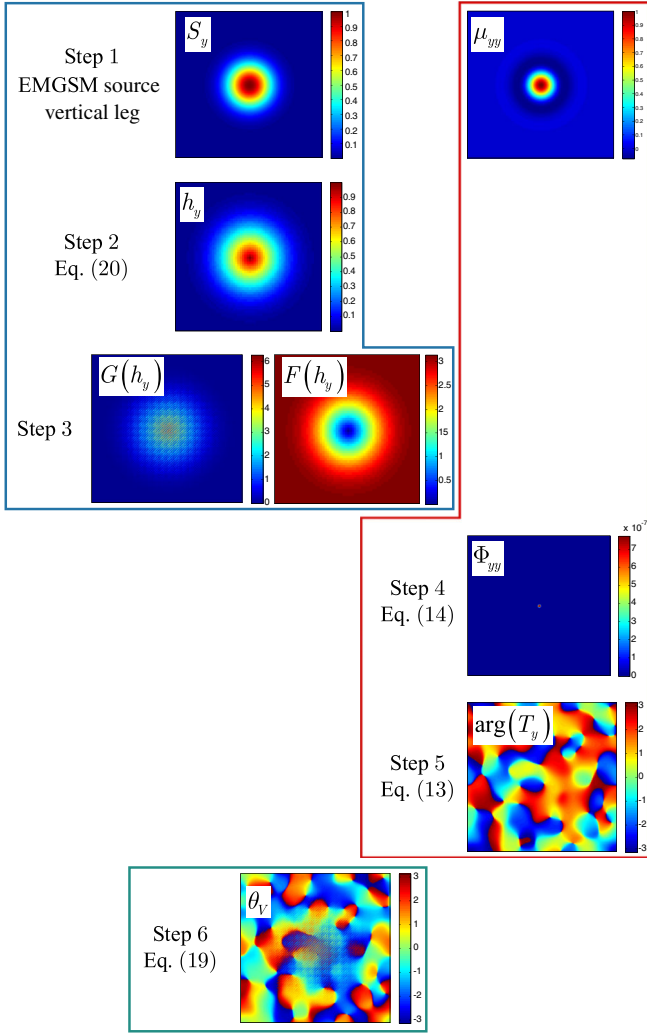
FIG. 2.   Screen synthesis process for producing the y (vertical) component of an EMGSM source.

popular mathematical software packages have correlated Gaussian random-number generators. Correlated Gaussian random numbers can also be produced by linearly transforming independent sequences of Gaussian random numbers [62].

IV. VALIDATION

A. Experimental procedure and data processing

ENUC and EMGSM sources are produced using the apparatus in Fig. 1 to demonstrate the flexibility and utility of the setup. The measured irradiances, I_x and I_y, from 5000 ENUC and EMGSM fields are used to compute the normalized spectral densities,

$$\tilde{S}_i(\boldsymbol{\rho}) = \frac{S_i(\boldsymbol{\rho})}{\max\{S_x(\boldsymbol{\rho}) + S_y(\boldsymbol{\rho})\}}, \quad (21)$$

and correlations of irradiance,

$$\tilde{\Gamma}_{ii}(\boldsymbol{\rho}_1, 0) = \frac{\Gamma_{ii}(\boldsymbol{\rho}_1, 0)}{\max\{\Gamma_{ii}(\boldsymbol{\rho}_1, 0)\}}$$

$$\tilde{\Gamma}_{ij}(\boldsymbol{\rho}_1, 0) = \frac{\Gamma_{ij}(\boldsymbol{\rho}_1, 0)}{\sqrt{\max\{\Gamma_{xx}(\boldsymbol{\rho}_1, 0)\Gamma_{yy}(\boldsymbol{\rho}_1, 0)\}}}, \quad (22)$$

where $\Gamma_{ij}(\boldsymbol{\rho}_1, \boldsymbol{\rho}_2) = \langle I_i(\boldsymbol{\rho}_1)I_j(\boldsymbol{\rho}_2)\rangle$. Each of the 5000 I_x's and I_y's are flat fielded and registered before computing the above moments. The experimental $\tilde{S}_i$ and $\tilde{\Gamma}_{ij}$ are then compared to the corresponding theoretical expressions (discussed below) to validate the proposed approach. It should be noted that I_x and I_y are physically separated at the camera or detector (not overlapped as shown in Fig. 1). The intention of this separation is to make calculating the spectral densities and correlations of irradiance more convenient. The experimental ENUC and EMGSM source parameters are reported in Table I. Figure 3 shows sample I_x's and I_y's for the ENUC [Figs. 3(a) and 3(b)] and EMGSM [Figs. 3(c) and 3(d)] sources.

ENUC sources exhibit self-focusing in the near field. The locations of the $\tilde{S}_i$ maxima are determined by $\boldsymbol{\gamma}_i$ [5,54]. Here, the $\tilde{S}_x$ and $\tilde{S}_y$ maxima occur off axis, shifted in the x and y directions, respectively (see Table I). EMGSM sources produce far-zone $\tilde{S}_i$'s with flat-topped profiles. The parameter M determines the flatness of $\tilde{S}_i$ [5,57].

In the experiments, the horizontal- and vertical-leg SLM gratings have a period of eight SLM pixels per sawtooth and are applied in both the x and y directions (i.e., diagonally). The BNS SLMs used in the experiments have a fill factor of 83.4% [46]. The dead space between the SLM pixels produces bright, sinclike, far-zone patterns coinciding with the zeroth diffraction orders in the horizontal and vertical legs of the apparatus. Using diagonal gratings moved the desired first orders away from the zeroth orders' bright sidelobes, thereby minimizing corruption of the resulting fields.

TABLE I.   Vector partially coherent source parameters.

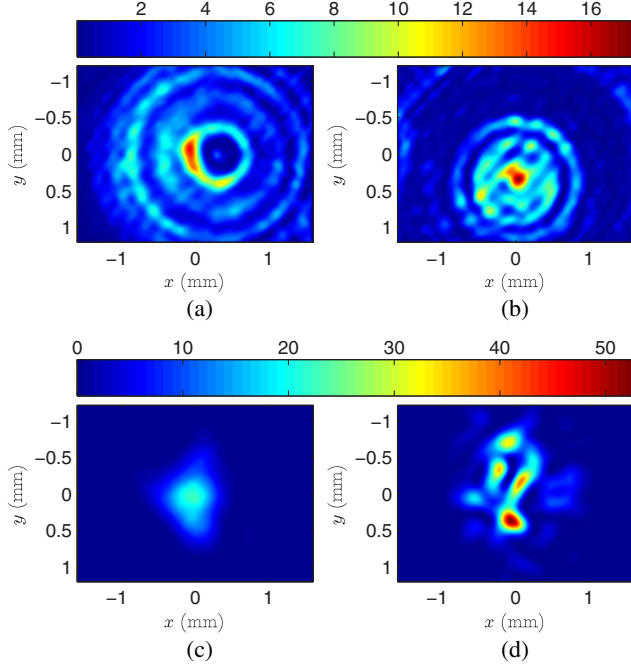|	ENUC	EMGSM
A_x	1	1.5
A_y	1	1
B_{xy}	0	0.5
σ_x (mm)	1	0.4
σ_y (mm)	1	0.8
δ_{xx} (mm)	0.7	0.6
δ_{yy} (mm)	0.6	0.6
δ_{xy} (mm)		0.6
$\boldsymbol{\gamma}_x$ (mm)	$\hat{x}0.6$	
$\boldsymbol{\gamma}_y$ (mm)	$\hat{y}0.7$	
M		10

FIG. 3.   Sample I_x's and I_y's. (a) ENUC I_x. (b) ENUC I_y. (c) EMGSM I_x. (d) EMGSM I_y. The units are in digital counts.

B. ENUC and EMGSM theoretical CSD matrices

The analytical expressions for the CSD matrix elements of an ENUC source corresponding to the experimental setup are

$$W_{ij}(\boldsymbol{\rho}_1,\boldsymbol{\rho}_2,z=f) = \frac{\exp[\frac{jk}{2f}(\rho_1^2 - \rho_2^2)]}{\lambda^2 f^2}$$

$$\times \iiiint\limits_{-\infty}^{\infty} W_{ij}(\boldsymbol{\rho}_1',\boldsymbol{\rho}_2') \exp\left[\frac{-jk}{2R}(\rho_1'^2 - \rho_2'^2)\right]$$

$$\times \exp\left[\frac{-jk}{f}(\boldsymbol{\rho}_1\cdot\boldsymbol{\rho}_1' - \boldsymbol{\rho}_2\cdot\boldsymbol{\rho}_2')\right] d^2\rho_1' d^2\rho_2', \tag{23}$$

where $f = 1.5$ m, $\lambda = 632.8$ nm, and W_{ij} in the integrand is the ENUC CSD function given in Eq. (6). The above integrals cannot be evaluated in closed form; however, they can be computed using the FFT algorithm.

As stated above, an interesting characteristic of ENUC sources is that they exhibit self-focusing in the near field [5,54]. To demonstrate this effect in the experiments, a $R = -3$ m phase curvature is applied to the horizontal- and vertical-leg SLMs, in addition to the ENUC phases given in Eq. (19).

Unlike ENUC sources, the theoretical EMGSM CSD matrix elements observed at the focus of a lens are easily derived in closed form:

$$W_{ij}(\boldsymbol{\rho}_1,\boldsymbol{\rho}_2,z=f)$$

$$= \frac{\exp[\frac{jk}{2f}(\rho_1^2 - \rho_2^2)] A_i A_j B_{ij}}{\lambda^2 f^2} \frac{1}{C_0}$$

$$\times \sum_{m=1}^{M} \frac{(-1)^{m-1}}{m} \binom{M}{n} \frac{\pi^2}{a_{i,ij}a_{j,ij} - b_{ij}^2}$$

$$\times \exp\left(-\frac{k}{4f^2} \frac{a_{j,ij}x_1^2 - 2b_{ij}x_1x_2 + a_{i,ij}x_2^2}{a_{i,ij}a_{j,ij} - b_{ij}^2}\right)$$

$$\times \exp\left(-\frac{k}{4f^2} \frac{a_{j,ij}y_1^2 - 2b_{ij}y_1y_2 + a_{i,ij}y_2^2}{a_{i,ij}a_{j,ij} - b_{ij}^2}\right), \tag{24}$$

where $a_{i,ij} = 1/(4\sigma_i^2) + b_{ij}$, $a_{j,ij} = 1/(4\sigma_j^2) + b_{ij}$, and $b_{ij} = 1/(2m\delta_{ij}^2)$.

The spectral densities are easy to compute using Eqs. (23) and (24), i.e., $S_i(\boldsymbol{\rho}) = W_{ii}(\boldsymbol{\rho},\boldsymbol{\rho})$. Since the fields are Gaussian distributed, the theoretical correlations of irradiance can be expressed in terms of Eqs. (23) and (24) by using the Gaussian-moment theorem [6,30,41,52]:

$$\langle I_i(\boldsymbol{\rho}_1)I_j(\boldsymbol{\rho}_2)\rangle = \langle E_i(\boldsymbol{\rho}_1)E_i^*(\boldsymbol{\rho}_1)E_j(\boldsymbol{\rho}_2)E_j^*(\boldsymbol{\rho}_2)\rangle$$

$$= \langle E_i(\boldsymbol{\rho}_1)E_j^*(\boldsymbol{\rho}_2)\rangle\langle E_i^*(\boldsymbol{\rho}_1)E_j(\boldsymbol{\rho}_2)\rangle$$

$$+ \langle E_i(\boldsymbol{\rho}_1)E_i^*(\boldsymbol{\rho}_1)\rangle\langle E_j(\boldsymbol{\rho}_2)E_j^*(\boldsymbol{\rho}_2)\rangle$$

$$= |W_{ij}(\boldsymbol{\rho}_1,\boldsymbol{\rho}_2)|^2 + S_i(\boldsymbol{\rho}_1)S_j(\boldsymbol{\rho}_2). \tag{25}$$

C. Results

Figures 4 and 5 show the near-field normalized spectral density and correlation of irradiance results for the ENUC source, respectively. Figures 6 and 7 show the corresponding far-field results for the EMGSM source. The first row in
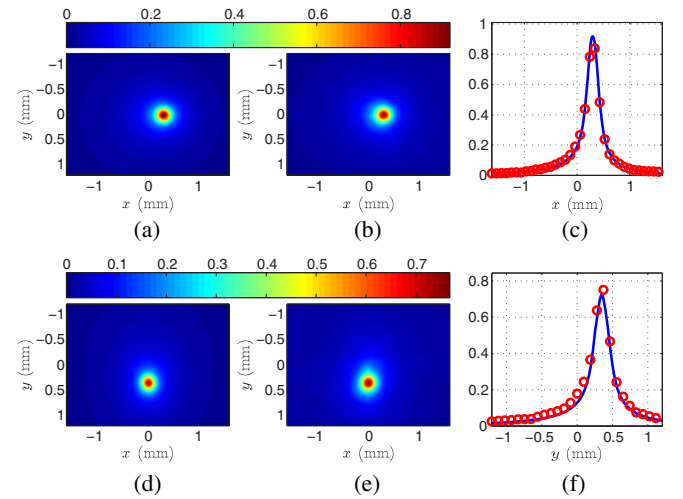

FIG. 4.   ENUC source near-field normalized spectral densities $\tilde{S}_x$ and $\tilde{S}_y$. (a) $\tilde{S}_x^{\text{thy}}$. (b) $\tilde{S}_x^{\text{exp}}$. (c) $\tilde{S}_x$ $y = 0$ slice, theory versus experiment. (d) $\tilde{S}_y^{\text{thy}}$. (e) $\tilde{S}_y^{\text{exp}}$. (f) $\tilde{S}_y$ $x = 0$ slice, theory versus experiment.

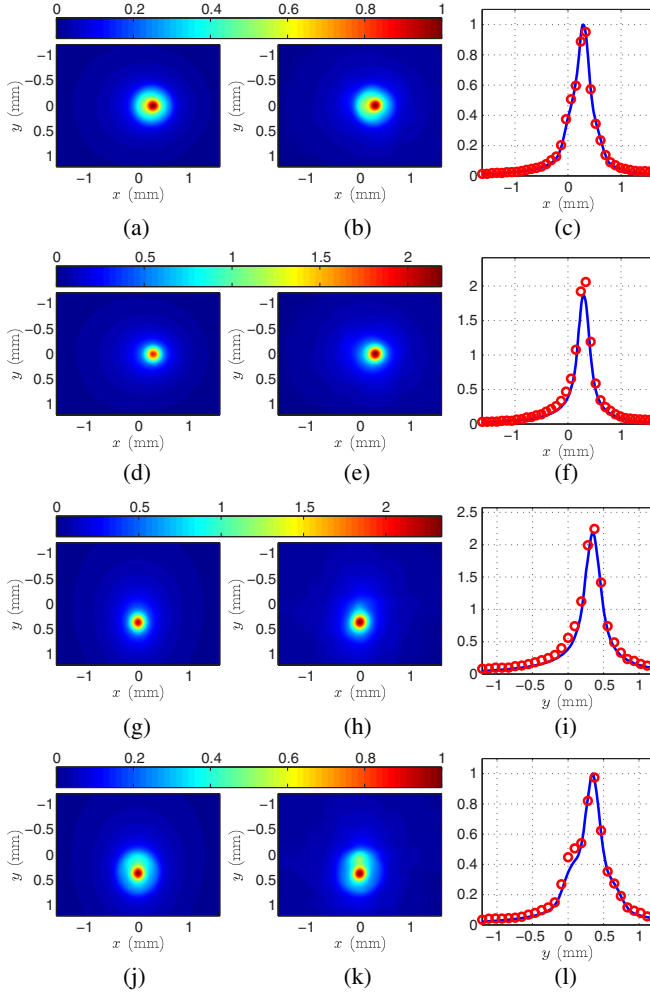FIG. 5. ENUC source near-field normalized correlations of irradiance $\tilde{\Gamma}_{xx}$, $\tilde{\Gamma}_{xy}$, $\tilde{\Gamma}_{yx}$, and $\tilde{\Gamma}_{yy}$. (a) $\tilde{\Gamma}_{xx}^{\text{thy}}$. (b) $\tilde{\Gamma}_{xx}^{\text{exp}}$. (c) $\tilde{\Gamma}_{xx}$ $y = 0$ slice, theory versus experiment. (d) $\tilde{\Gamma}_{xy}^{\text{thy}}$. (e) $\tilde{\Gamma}_{xy}^{\text{exp}}$. (f) $\tilde{\Gamma}_{xy}$ $y = 0$ slice, theory versus experiment. (g) $\tilde{\Gamma}_{yx}^{\text{thy}}$. (h) $\tilde{\Gamma}_{yx}^{\text{exp}}$. (i) $\tilde{\Gamma}_{yx}$ $x = 0$ slice, theory versus experiment. (j) $\tilde{\Gamma}_{yy}^{\text{thy}}$. (k) $\tilde{\Gamma}_{yy}^{\text{exp}}$. (l) $\tilde{\Gamma}_{yy}$ $x = 0$ slice, theory versus experiment.

the spectral-density figures (Figs. 4 and 6) shows (a) the theoretical $\tilde{S}_x^{\text{thy}}$, (b) the experimental $\tilde{S}_x^{\text{exp}}$, and (c) the $y = 0$ slice of $\tilde{S}_x$ theory (the solid blue trace) versus experiment (the red circles), respectively. The second row [(d), (e), and (f)] shows the same results for $\tilde{S}_y$, except for (f), which reports the $x = 0$ slice.

The correlation of irradiance figures (Figs. 5 and 7) are oriented in a similar manner to the spectral-density results. The first and second rows show the theoretical [(a) and (d)], experimental [(b) and (e)], and $y = 0$ slice of theory (the solid blue trace) versus experiment (the red circles) [(c) and (f)] results for $\tilde{\Gamma}_{xx}$ and $\tilde{\Gamma}_{xy}$, respectively. The third and fourth rows show the same results for $\tilde{\Gamma}_{yx}$ and $\tilde{\Gamma}_{yy}$, except for (i) and (l), which report the $x = 0$ slices.

Except for a few minor discrepancies, e.g., Figs. 5(f), 5(l), and 6(c), the agreement between the experimental and
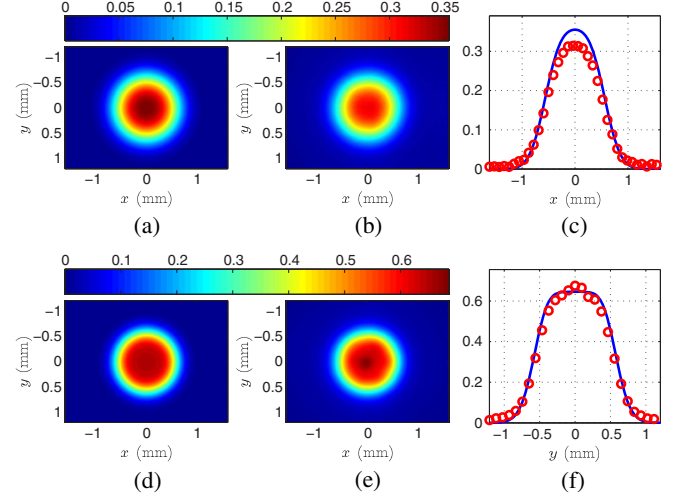

FIG. 6. EMGSM source far-zone normalized spectral densities $\tilde{S}_x$ and $\tilde{S}_y$. (a) $\tilde{S}_x^{\text{thy}}$. (b) $\tilde{S}_x^{\text{exp}}$. (c) $\tilde{S}_x$ $y = 0$ slice, theory versus experiment. (d) $\tilde{S}_y^{\text{thy}}$. (e) $\tilde{S}_y^{\text{exp}}$. (f) $\tilde{S}_y$ $x = 0$ slice, theory versus experiment.

theoretical results is excellent. These results validate the proposed approach. It should be noted that EGSM vortex [32] and electromagnetic Bessel-Gaussian Schell-model beams [11] are also produced as part of this study. The results are similar to those for ENUC and EMGSM sources; they are omitted here for the sake of brevity.

D. $\arg(B_{xy})$

One parameter that has been difficult to control is $\arg(B_{xy})$, which is required if one desires to generate elliptically polarized sources. Precise control of this term requires that the OPD between the horizontal and vertical legs of the apparatus be known and, most importantly, stable. The OPD between the legs can vary significantly due to slight variations in temperature or small vibrations.

Unfortunately, we are not able to stabilize the OPD of our system. In our most recent attempt, we try to actively correct the system OPD using a three-bin phase-shifting interferometer and a variable retarder operating in a closed loop. The OPD drift is too fast to correct. Subsequent measurement of our system OPD finds that it varies randomly over 0.5 waves (roughly 300 nm) and faster than 120 Hz. Our inability to control $\arg(B_{xy})$ is a limitation of our equipment, not the proposed approach. The control of $\arg(B_{xy})$ is left to future work.

V. DESIGN CONSIDERATIONS

Before concluding, it is worth discussing some key aspects of the proposed approach which must be considered when designing or building a system like that in Fig. 1 for a specific application. Two of these aspects have already been discussed—controlling the OPD between the horizontal and
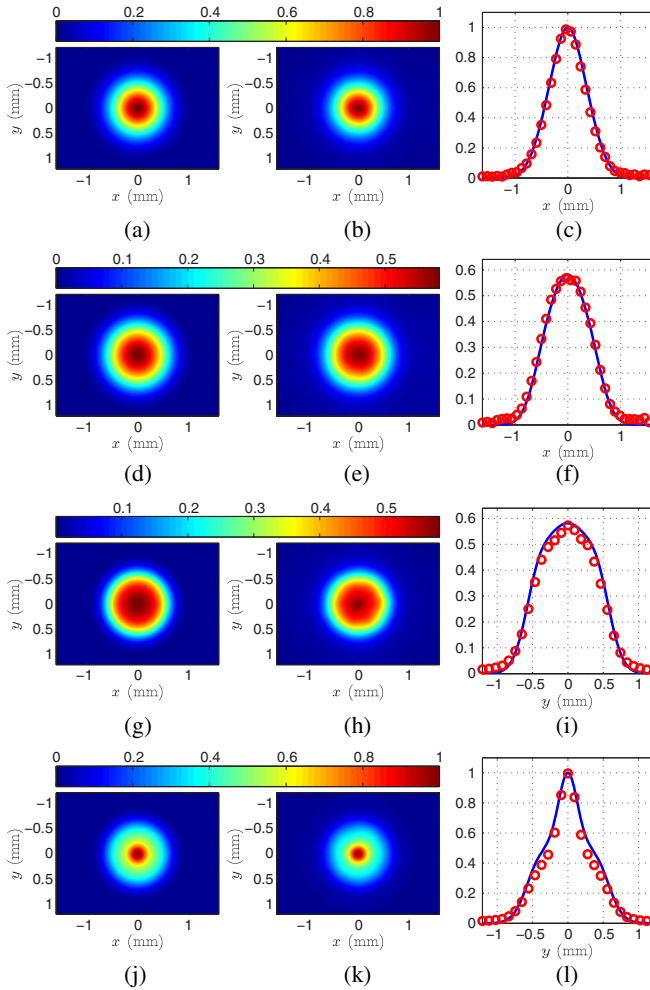
FIG. 7. EMGSM source far-zone normalized correlations of irradiance $\tilde{\Gamma}_{xx}$, $\tilde{\Gamma}_{xy}$, $\tilde{\Gamma}_{yx}$, and $\tilde{\Gamma}_{yy}$. (a) $\tilde{\Gamma}_{xx}^{\text{thy}}$. (b) $\tilde{\Gamma}_{xx}^{\text{exp}}$. (c) $\tilde{\Gamma}_{xx}$ $y = 0$ slice, theory versus experiment. (d) $\tilde{\Gamma}_{xy}^{\text{thy}}$. (e) $\tilde{\Gamma}_{xy}^{\text{exp}}$. (f) $\tilde{\Gamma}_{xy}$ $y = 0$ slice, theory versus experiment. (g) $\tilde{\Gamma}_{yx}^{\text{thy}}$. (h) $\tilde{\Gamma}_{yx}^{\text{exp}}$. (i) $\tilde{\Gamma}_{yx}$ $x = 0$ slice, theory versus experiment. (j) $\tilde{\Gamma}_{yy}^{\text{thy}}$. (k) $\tilde{\Gamma}_{yy}^{\text{exp}}$. (l) $\tilde{\Gamma}_{yy}$ $x = 0$ slice, theory versus experiment.

vertical legs of the MZI and the coherence length of the light source. In addition to these factors, the size D, pixel pitch Δ, and type of SLM also play an important role in the types of sources that can be generated.

A. SLM size D

Clearly, sources with correlation or beam widths (δ and σ, respectively) greater than D cannot be accurately generated. Even sources with $\delta, \sigma \approx D$ will have correlation functions μ or spectral densities S that are driven by the shape of the SLM's active area. Therefore, D sets the effective "coherent" and "maximum" source sizes. In practice, both S and μ should "fit" comfortably on the SLM face. An empirically derived criterion which ensures this fit is that both μ and $\sqrt{S}$ should be no greater than 1% of their maximum values at the edges of the SLM.

B. SLM pitch Δ

To adequately sample or represent μ requires $\Delta < \delta/5$, where δ, in this context, is the $1/e$ point or first zero crossing of μ (whichever is appropriate). Sources with correlation radii $\delta < 5\Delta$ are not accurately produced, making 5Δ the effective "incoherent" limit of the SLM. Similarly, adequate sampling of S generally requires that $\Delta < \sigma/(5L)$, where σ is the $1/e$ point or first zero location of $\sqrt{S}$ (whichever is appropriate) and L is the sawtooth-grating period. This requirement is more stringent than the correlation condition because SLM pixels are binned to form the sawtooth grating (eight pixels are used in this work). Thus, the amplitude of the desired source is generally harder to produce than is the phase [47,51]. The requirement that $\sigma > 5L\Delta$ sets the effective "minimum" source size of the SLM.

The grating period L affects system performance in two competing ways. A large L better approximates a continuous sawtooth and results in more precise amplitude control. Recall that the expression relating sawtooth-grating height to the field in the first diffraction order [Eq. (18)] requires that $L > 4$. L also affects the angular separation of the diffraction orders:

$$\sin \theta_m = \frac{m\lambda}{L\Delta}, \tag{26}$$

where m is the order number [63]. Clearly, L and θ_m are inversely related. L must therefore be chosen so that the field's amplitude can be accurately produced, while also providing a large enough angular separation of the orders such that the desired first order can be passed by a spatial filter with little corruption from the $m \neq 1$ orders.

C. SLM type

Many different types of SLMs exist [63]. The two most popular are liquid-crystal (LC) SLMs (the type used here) and MEMS SLMs (also known as segmented deformable mirrors). Both have pros and cons which are briefly discussed here. LC SLMs generally possess a large number of small pixels—the current state of the art is a 10 megapixel (4094×2464) SLM with a 3.74-μm pitch [64]. The sheer number and size of the pixels in modern LC SLMs permits practically any partially coherent source to be generated. The major drawback of LC SLMs is speed, with the fastest operating at about 1 kHz. Note that most LC SLMs operate well below 1 kHz; the 10-megapixel SLM mentioned previously operates at 24 Hz [64].

MEMS SLMs, on the other hand, generally possess a much smaller number of much larger pixels (or actuators). The current state of the art in MEMS SLMs is a 4092-actuator (64×64) device with a 400-μm pitch [65]. When one considers the importance of SLM size and pitch in producing partially coherent sources, it is clear that MEMS SLMs cannot match the range of LC SLMs. MEMS SLMs,

however, are orders of magnitude faster than their LC counterparts, e.g., the 4092-actuator MEMS device mentioned previously operates at 10 kHz [65].

Choosing which type of SLM to employ in the apparatus in Fig. 1 comes down to the importance of speed. If speed is of lesser importance than flexibility in the application, LC SLMs are the best choice. If, on the other hand, speed is paramount, MEMS SLMs are the better option.

D. Design optimization

What makes the apparatus in Fig. 1 very powerful is the ability to generate many different types of vector partially coherent sources using phase-only SLMs and a simple optical setup. The range of sources that can be produced is much greater than existing systems which use separate optical components to manipulate beam shape and coherence. The most significant drawback of the proposed approach over existing partially coherent source generators, particularly those which use rotating ground-glass diffusers and amplitude filters, is speed. As stated above, if speed is paramount, MEMS SLMs can be used instead of LC SLMs at the expense of flexibility.

It should be noted that the apparatus in Fig. 1 is built for proof-of-concept purposes only, with no particular application in mind. Thus, the total size of the system (its footprint) has not been optimized. The largest components (in terms of physical size) in Fig. 1 are the spatial filters. Long-focal-length plano-convex lenses are used here solely for ease of setup, alignment (i.e., to minimize aberrations), and cost. By changing the layout of the system and employing standard optical design techniques [66,67], the entire apparatus could be made to fit within a 1-m^2 area.

VI. CONCLUSION

An alternative design for generating vector partially coherent sources is presented. In contrast to existing designs which use separate optical components to manipulate beam shape and spatial coherence (commonly, amplitude filters and ground-glass diffusers or SLMs), the system described here uses only SLMs to control these aspects of the field. In addition to having a simpler optical setup, this improvement significantly increases the flexibility of vector partially coherent source generators by permitting many different types of sources to be produced without physically changing the apparatus.

System design is thoroughly discussed in Sec. II. Section III presents the theory underpinning the design, namely, the MPS technique, screen synthesis for both Schell-model and non-Schell-model sources, and phase-only field control. Section IV demonstrates the effectiveness and flexibility of the proposed system by producing ENUC and EMGSM sources, neither of which, to the authors' knowledge, have been physically generated

before. The apparatus is validated by comparing experimental ENUC and EMGSM results to theoretical predictions. The agreement between theory and experiment is excellent. Lastly, key aspects of system design—the effects of SLM size, pixel pitch, and SLM type on partially coherent source generation—are discussed.

The system design and subsequent approach for generating vector partially coherent sources presented in this paper will be useful in any application where control over beam shape, spatial coherence, and polarization is required. These applications include—but are not limited to—free-space optical communications, directed energy, remote sensing, manufacturing, and medicine.

ACKNOWLEDGMENTS

[1] E. Wolf, Unified theory of coherence and polarization of random electromagnetic beams, Phys. Lett. A **312**, 263 (2003).

[2] E. Wolf, *Introduction to the Theory of Coherence and Polarization of Light* (Cambridge University, Cambridge, England, 2007).

[3] F. Gori, M. Santarsiero, S. Vicalvi, R. Borghi, and G. Guattari, Beam coherence-polarization matrix, Pure Appl. Opt. **7**, 941 (1998).

[4] G. Gbur and T. D. Visser, in *Progress in Optics*, Vol. 55, edited by Emil Wolf (Elsevier, New York, 2010), Chap. 5, pp. 285–341.

[5] O. Korotkova, *Random Light Beams: Theory and Applications* (CRC, Boca Raton, 2014).

[6] *Vectorial Optical Fields: Fundamentals and Applications*, edited by Q. Zhan (World Scientific, Singapore, 2014).

[7] M. Yao, I. Toselli, and O. Korotkova, Propagation of electromagnetic stochastic beams in anisotropic turbulence, Opt. Express **22**, 31608 (2014).

[8] G. Gbur, Partially coherent beam propagation in atmospheric turbulence, J. Opt. Soc. Am. A **31**, 2038 (2014).

[9] M. Salem, O. Korotkova, A. Dogariu, and E. Wolf, Polarization changes in partially coherent electromagnetic beams propagating through turbulent atmosphere, Waves Random Media **14**, 513 (2004).

[10] S. Avramov-Zamurovic, C. Nelson, R. Malek-Madani, and O. Korotkova, Polarization-induced reduction in scintillation of optical beams propagating in simulated turbulent atmospheric channels, Waves Random Complex Media **24**, 452 (2014).

[11] S. Avramov-Zamurovic, C. Nelson, S. Guth, O. Korotkova, and R. Malek-Madani, Experimental study of electromagnetic Bessel-Gaussian Schell model beams propagating in a turbulent channel, Opt. Commun. **359**, 207 (2016).

[12] C. Nelson, S. Avramov-Zamurovic, O. Korotkova, S. Guth, and R. Malek-Madani, Scintillation reduction in pseudo multi-Gaussian Schell model beams in the maritime environment, Opt. Commun. **364**, 145 (2016).

[13] F. Wang, X. Liu, and Y. Cai, Propagation of partially coherent beam in turbulent atmosphere: a review, Prog. Electromagn. Res. **150**, 123 (2015).

[14] O. Korotkova and N. Farwell, Effect of oceanic turbulence on polarization of stochastic beams, Opt. Commun. **284**, 1740 (2011).

[15] O. Korotkova, L. C. Andrews, and R. L. Phillips, Model for a partially coherent Gaussian beam in atmospheric turbulence with application in lasercom, Opt. Eng. **43**, 330 (2004).

[16] K. Drexler, M. Roggemann, and D. Voelz, Use of a partially coherent transmitter beam to improve the statistics of received power in a free-space optical communication system: Theory and experimental results, Opt. Eng. **50**, 025002 (2011).

[17] S. Sahin, Z. Tong, and O. Korotkova, Sensing of semi-rough targets embedded in atmospheric turbulence by means of stochastic electromagnetic beams, Opt. Commun. **283**, 4512 (2010).

[18] Y. Cai, O. Korotkova, H. T. Eyyuboglu, and Y. Baykal, Active laser radar systems with stochastic electromagnetic beams in turbulent atmosphere, Opt. Express **16**, 15834 (2008).

[19] J. Liu, L. Bi, P. Yang, and G. W. Kattawar, Scattering of partially coherent electromagnetic beams by water droplets and ice crystals, J. Quant. Spectrosc. Radiat. Transfer **134**, 74 (2014).

[20] Y. Zhang and D. Zhao, The coherence and polarization properties of electromagnetic rectangular Gaussian Schell-model sources scattered by a deterministic medium, J. Opt. **16**, 125709 (2014).

[21] T. van Dijk, D. G. Fischer, T. D. Visser, and E. Wolf, Effects of Spatial Coherence on the Angular Distribution of Radiant Intensity Generated by Scattering on a Sphere, Phys. Rev. Lett. **104**, 173902 (2010).

[22] F. J. Torcal-Milla and L. M. Sanchez-Brea, Gaussian-Schell-model beams propagating through rough gratings, J. Opt. Soc. Am. A **28**, 308 (2011).

[23] D. G. Fischer, T. van Dijk, T. D. Visser, and E. Wolf, Coherence effects in Mie scattering, J. Opt. Soc. Am. A **29**, 78 (2012).

[24] M. W. Hyde IV, Physical optics solution for the scattering of a partially coherent wave from a circular cylinder, Opt. Commun. **338**, 233 (2015).

[25] M. W. Hyde, A. E. Bogle, and M. J. Havrilla, Scattering of a partially-coherent wave from a material circular cylinder, Opt. Express **21**, 32327 (2013).

[26] Y. Wang, S. Yan, D. Kuebel, and T. D. Visser, Dynamic control of light scattering using spatial coherence, Phys. Rev. A **92**, 013806 (2015).

[27] Y. Wang, H. F. Schouten, and T. D. Visser, Tunable, anomalous Mie scattering using spatial coherence, Opt. Lett. **40**, 4779 (2015).

[28] Z. Mei and O. Korotkova, Random light scattering by collections of ellipsoids, Opt. Express **20**, 29296 (2012).

[29] Y. Zhang and D. Zhao, Scattering of multi-Gaussian Schell-model beams on a random medium, Opt. Express **21**, 24781 (2013).

[30] Y. Chen, F. Wang, L. Liu, C. Zhao, Y. Cai, and O. Korotkova, Generation and propagation of a partially coherent vector beam with special correlation functions, Phys. Rev. A **89**, 013801 (2014).

[31] F. Wang, Y. Cai, Y. Dong, and O. Korotkova, Experimental generation of a radially polarized beam with controllable spatial coherence, Appl. Phys. Lett. **100**, 051108 (2012).

[32] X. Liu, F. Wang, L. Liu, C. Zhao, and Y. Cai, Generation and propagation of an electromagnetic Gaussian Schell-model vortex beam, J. Opt. Soc. Am. A **32**, 2058 (2015).

[33] Y. Chen, F. Wang, J. Yu, L. Liu, and Y. Cai, Vector Hermite-Gaussian correlated Schell-model beam, Opt. Express **24**, 15232 (2016).

[34] T. Shirai, O. Korotkova, and E. Wolf, A method of generating electromagnetic Gaussian Schell-model beams, J. Opt. A **7**, 232 (2005).

[35] M. Santarsiero, R. Borghi, and V. Ramírez-Sánchez, Synthesis of electromagnetic Schell-model sources, J. Opt. Soc. Am. A **26**, 1437 (2009).

[36] G. Piquero, F. Gori, P. Romanini, M. Santarsiero, R. Borghi, and A. Mondello, Synthesis of partially polarized Gaussian Schell-model sources, Opt. Commun. **208**, 9 (2002).

[37] A. S. Ostrovsky, G. Rodríguez-Zurita, C. Meneses-Fabián, M. Á. Olvera-Santamaría, and C. Rickenstorff-Parrao, Experimental generating the partially coherent and partially polarized electromagnetic source, Opt. Express **18**, 12864 (2010).

[38] A. S. Ostrovsky, M. A. Olvera, C. Rickenstorff, G. Martínez-Niconoff, and V. Arrizón, Generation of a secondary electromagnetic source with desired statistical properties, Opt. Commun. **283**, 4490 (2010).

[39] I. Vidal, E. J. S. Fonseca, and J. M. Hickmann, Light polarization control during free-space propagation using coherence, Phys. Rev. A **84**, 033836 (2011).

[40] P. De Santis, F. Gori, G. Guattari, and C. Palma, An example of a Collett-Wolf source, Opt. Commun. **29**, 256 (1979).

[41] Y. Cai, Y. Chen, and F. Wang, Generation and propagation of partially coherent beams with nonconventional correlation functions: A review, J. Opt. Soc. Am. A **31**, 2083 (2014).

[42] T. Shirai and E. Wolf, Coherence and polarization of electromagnetic beams modulated by random phase screens and their changes on propagation in free space, J. Opt. Soc. Am. A **21**, 1907 (2004).

[43] A. S. Ostrovsky, G. Martínez-Niconoff, V. Arrizón, P. Martínez-Vara, M. A. Olvera-Santamaría, and C. Rickenstorff-Parrao, Modulation of coherence and polarization using liquid crystal spatial light modulators, Opt. Express **17**, 5257 (2009).

[44] L. Mandel and E. Wolf, *Optical Coherence and Quantum Optics* (Cambridge University, Cambridge, England, 1995).

[45] J. W. Goodman, *Statistical Optics*, 2nd ed. (Wiley, New York, 2015).

[46] Boulder Nonlinear Systems, Inc., Spatial Light Modulators—XY Series (retrieved on July 6, 2016).

[47] M. W. Hyde IV, S. Basu, D. G. Voelz, and X. Xiao, Generating partially coherent Schell-model sources using a modified phase screen approach, Opt. Eng. **54**, 120501 (2015).

[48] Lumenera Corporation, Lw130R and Lw135R Very Low Noise Research—Grade 1.4 Megapixel USB 2.0 Camera for Custom OEM Applications (retrieved on July 6, 2016).

[49] D. Voelz, X. Xiao, and O. Korotkova, Numerical modeling of Schell-model beams with arbitrary far-field patterns, Opt. Lett. **40**, 352 (2015).

[50] S. Basu, M. W. Hyde, X. Xiao, D. G. Voelz, and O. Korotkova, Computational approaches for generating electromagnetic Gaussian Schell-model sources, Opt. Express **22**, 31691 (2014).

[51] M. W. Hyde, S. Basu, D. G. Voelz, and X. Xiao, Experimentally generating any desired partially coherent Schell-model source using phase-only control, J. Appl. Phys. **118**, 093102 (2015).

[52] J. W. Goodman, *Speckle Phenomena in Optics: Theory and Applications* (Roberts & Company, Englewood, CO, 2007).

[53] M. W. Hyde IV, S. Basu, X. Xiao, and D. G. Voelz, Producing any desired far-field mean irradiance pattern using a partially-coherent Schell-model source, J. Opt. **17**, 055607 (2015).

[54] Z. Tong and O. Korotkova, Electromagnetic nonuniformly correlated beams, J. Opt. Soc. Am. A **29**, 2154 (2012).

[55] M. C. Roggemann and B. M. Welsh, *Imaging Through Turbulence* (CRC, Boca Raton, 1996).

[56] D. S. Watkins, *Fundamental of Matrix Computations*, 2nd ed. (Wiley, New York, 2002).

[57] Z. Mei, O. Korotkova, and E. Shchepakina, Electromagnetic multi-Gaussian Schell-model beams, J. Opt. **15**, 025705 (2013).

[58] C. A. Mack, Generating random rough edges, surfaces, and volumes, Appl. Opt. **52**, 1472 (2013).

[59] X. Xiao and D. Voelz, Wave optics simulation approach for partial spatially coherent beams, Opt. Express **14**, 6986 (2006).

[60] E. Bolduc, N. Bent, E. Santamato, E. Karimi, and R. W. Boyd, Exact solution to simultaneous intensity and phase encryption with a single phase-only hologram, Opt. Lett. **38**, 3546 (2013).

[61] J. A. Davis, D. M. Cottrell, J. Campos, M. J. Yzuel, and I. Moreno, Encoding amplitude information onto phase-only filters, Appl. Opt. **38**, 5004 (1999).

[62] S. Kay, *Intuitive Probability and Random Processes using* MATLAB® (Springer, New York, 2006).

[63] J. W. Goodman, *Introduction to Fourier Optics*, 3rd ed. (Roberts & Company, Englewood, CO, 2005).

[64] Holoeye Photonics AG, SLM Spatial Light Modulators (retrieved on November 8, 2016).

[65] Boston Micromachines Corporation, +K-DM Family Specification Sheet (retrieved on November 8, 2016).

[66] M. J. Kidger, *Fundamental Optical Design* (SPIE, Bellingham, WA, 2001).

[67] M. J. Kidger, *Intermediate Optical Design* (SPIE, Bellingham, WA, 2004).